Numerical study of bulk acoustofluidic devices driven by thin-film transducers and whole-system resonance modes[a)]

André G. Steckel and Henrik Bruus[b)]

Department of Physics, Technical University of Denmark, DTU Physics Building 309, DK-2800 Kongens Lyngby, Denmark

ABSTRACT:

In bulk acoustofluidic devices, acoustic resonance modes for fluid and microparticle handling are traditionally excited by bulk piezoelectric (PZE) transducers. In this work, it is demonstrated by numerical simulations in three dimensions that integrated PZE thin-film transducers, constituting less than 0.1% of the bulk device, work equally well. The simulations are performed using a well-tested and experimentally validated numerical model. A water-filled straight channel embedded in a mm-sized bulk glass chip with a 1-μm-thick thin-film transducer made of $Al_{0.6}Sc_{0.4}N$ is presented as a proof-of-concept example. The acoustic energy, radiation force, and microparticle focusing times are computed and shown to be comparable to those of a conventional bulk silicon-glass device actuated by a bulk lead-zirconate-titanate transducer. The ability of thin-film transducers to create the desired acoustofluidic effects in bulk acoustofluidic devices relies on three physical aspects: the in-plane-expansion of the thin-film transducer under the applied orthogonal electric field, the acoustic whole-system resonance of the device, and the high Q-factor of the elastic solid, constituting the bulk part of the device. Consequently, the thin-film device is remarkably insensitive to the Q-factor and resonance properties of the thin-film transducer.

© 2021 Author(s). *All article content, except where otherwise noted, is licensed under a Creative Commons Attribution (CC BY) license (http://creativecommons.org/licenses/by/4.0/).* https://doi.org/10.1121/10.0005624

(Received 30 January 2021; revised 16 June 2021; accepted 24 June 2021; published online 29 July 2021)

[Editor: Kedar Chitale]   Pages: 634–645

I. INTRODUCTION

An increasing number of microscale ultrasound acoustofluidic devices are used for applications within clinical diagnostics, biology, and forensic sciences.[1–5] Examples include but are not limited to rapid sepsis diagnostics by detection of bacteria in blood,[6] enrichment of prostate cancer cells in blood,[7] high-throughput cytometry and multiple-cell handling,[8,9] cell synchronization,[10] single-cell patterning and manipulation,[11,12] and size-independent sorting of cells.[13] Furthermore, acoustofluidics has been used for massively parallel force microscopy on biomolecules,[14] acoustic tweezing,[15–18] and noncontact microfluidic trapping and particle enrichment.[19]

Most applications rely on one of two basic methods for exciting the ultrasound field. One method is based on surface acoustic waves, excited by interdigitated metallic electrodes positioned on the surface of a piezoelectric (PZE) substrate. The other method relies on bulk acoustic waves excited in liquid-filled acoustic microchannels embedded in acoustically hard bulk devices by an attached bulk transducer that makes up 10%–50% volume-per-volume (v/v) of the device[20] or in microchannels with a thin silicon-membrane lid driven by a lead-zirconate-titanate (PZT) thin film that makes up around 15% v/v of the actuated

membrane, which is excited while leaving the bulk part of the device inert.[21]

Recently, the bulk-acoustic-wave method has been extended by the concept of whole-system ultrasound resonances (WSUR) in which the resonant acoustic modes are defined by the whole system and not just the microcavities.[22,23] In this paper, we extend the WSUR concept by substituting the large bulk PZE transducer by a tiny PZE thin-film transducer integrated on the surface of the device and constituting less than 0.1% v/v of the resulting globally actuated device, a volume ratio 2 orders of magnitude smaller than any previous device.

Integrated thin-film PZE transducers have been used extensively for actuating electromechanical systems and are often made of aluminum nitride (AlN). Thin-film transducers made of AlN are structurally and chemically stable, have a low dielectric and mechanical loss, and are compatible with standard silicon-based complementary metal-oxide semiconductor (CMOS) microfabrication techniques. Academic applications of AlN thin-film transducers include radio-frequency (RF) filters,[24] suspended microchannel resonators,[25] contour mode resonators,[26] switches,[27,28] and accelerometers.[29] AlN thin films have been deposited on substrates of sapphire, crystal quartz, fused silica, and silicon,[30] and 30-μm-thick Si membranes.[31,32] Commercially, AlN-sputtered thin films are used in thin-film bulk-wave acoustic resonator filters.[33] However, hitherto thin-film transducers have not yet been applied in generic MHz bulk

acoustofluidic devices other than the aforementioned specialized silicon-membrane device.[21]

In this paper, based on a well-tested and experimentally validated numerical model,[23,34,35] we demonstrate by three-dimensional (3D) numerical simulations that generic bulk glass chips with integrated PZE thin-film transducers constituting less than 0.1% v/v of the system, as sketched in Fig. 1, form devices with an acoustofluidic response on par with that obtained in a conventional silicon-glass device actuated by a bulk-PZT transducer using equivalent model assumptions. This result offers several advantages for the practical application of thin-film transducers within acoustofluidics: Thin-film devices do not depend on resonance properties of the thin-film transducer itself, they require no gluing, and can be fabricated by well-controlled reproducible microfabrication techniques subject to parallel mass-fabrication processes. We use 3D modeling to capture the axial variations observed experimentally even in straight, rectangular acoustofluidic channels.[36]

The paper is organized as follows: In Sec. II, we briefly summarize the theory and numerical model used throughout the paper. In Sec. III, we present a proof-of-concept example showing that a thin-film acoustofluidic bulk device performs on par with a conventional bulk-transducer bulk device. In Sec. IV, we discuss the physical principle of the thin-film transduction process; robustness of the device to the material, thickness, and quality factor of the thin-film transducer; role of the shape of the thin-film-transducer electrodes, spatial regularity, and sensitivity of the device to shifts in the channel position away from exact centering in the glass chip. Finally, in Sec. V, we present our conclusions.

II. THEORY

Throughout this work, we use the theory and numerical model developed by Skov *et al.*,[34] including the effective

FIG. 1. (Color online) (a) A sketch of the *yz*-plane cross section of the long, straight thin-film driven device consisting of an elastic solid (gray) of width W_{sl} and height H_{sl}, an embedded fluid-filled microchannel (blue) of width W_{fl} and height H_{fl}, and an attached thin-film transducer (beige) of width W_{sl} and small height $H_{thf} \approx 0.001 H_{sl}$. (b) A zoom-in on the thin-film transducer (beige) showing its grounded top electrode (black, of width W_{sl} and potential zero) and split-bottom electrode (red "+" and blue "−" of width $W_{el}^{\pm}$ and potential $\pm\frac{1}{2}\varphi_0$), made to excite the antisymmetric half-wave-like resonance mode.

boundary layer theory for the fluid domain by Bach and Bruus,[37] as briefly summarized in this section. This model is well-tested and experimentally validated for acoustofluidic devices,[23,34,35] and although it was originally stated for bulk-PZT transducers, the model is trivially extended to describe other types of PZE transducers, including thin-film transducers.

A. Governing equations for the time-harmonic fields

We consider a time-harmonic electric potential $\tilde{\varphi}(\boldsymbol{r}, t)$, which excites the PZE transducer and induces a displacement field $\tilde{\boldsymbol{u}}_1(\boldsymbol{r}, t)$ in the solids that, in turn, leads to an acoustic pressure $\tilde{p}_1(\boldsymbol{r}, t)$ in the fluid channel. All of these fields $\tilde{F}(\boldsymbol{r}, t)$ separate into a complex-valued amplitude $F(\boldsymbol{r})$ and complex time-harmonic phase factor with frequency f,

$$\tilde{F}(\boldsymbol{r}, t) = F(\boldsymbol{r}) \, e^{-i\omega t}, \quad \omega = 2\pi f. \tag{1}$$

The phase factor $e^{-i\omega t}$ cancels out in the following linear governing equations, leaving just the amplitude fields.

The first-order perturbation theory implies that the acoustic pressure p_1 in the fluid is governed by the Helmholtz equation with a damping coefficient Γ_{fl},[34]

$$\nabla^2 p_1 = -\frac{\omega^2}{c_{fl}^2}(1 + i\Gamma_{fl}) p_1, \quad \Gamma_{fl} = \left(\frac{4}{3}\eta_{fl} + \eta_{fl}^b\right)\omega\kappa_{fl}, \tag{2}$$

where c_{fl} is the speed of sound, ρ_{fl} is the density, $\kappa_{fl} = (\rho_{fl}c_{fl}^2)^{-1}$ is the isentropic compressibility, and η_{fl} and η_{fl}^b are the dynamic and bulk viscosity of the fluid, respectively; see Table S1 in the supplementary material.[38] The pressure gradient governs the acoustic fluid velocity $\boldsymbol{v}_1^{fl}$,

$$\boldsymbol{v}_1^{fl} = -i\frac{1 - i\Gamma_{fl}}{\omega\rho_{fl}} \boldsymbol{\nabla} p_1. \tag{3}$$

For the linear PZE transducer (of either $Al_{1-x}Sc_xN$, AlN, or PZT), the electrical potential φ is governed by Gauss's law for a linear dielectric without free charges,[34]

$$\boldsymbol{\nabla} \cdot \boldsymbol{D} = 0, \tag{4}$$

where $\boldsymbol{D}$ is the electric displacement field, including a purely electric part $-(1 + i\Gamma_\varepsilon)\boldsymbol{\varepsilon} \cdot \boldsymbol{\nabla}\varphi$, in which Γ_ε is a small damping coefficient, and $\boldsymbol{\varepsilon}$ is the dielectric tensor. The governing equation for the mechanical displacement field $\boldsymbol{u}_1$ in a linear elastic solid (including the PZE) with density ρ_{sl} is the weakly damped Cauchy equation,[34,39]

$$-(1 + i\Gamma_{sl})\rho_{sl}\omega^2 \boldsymbol{u}_1 = \boldsymbol{\nabla} \cdot \boldsymbol{\sigma}_{sl}, \tag{5}$$

where Γ_{sl} is a small damping coefficient. Using the Voigt notation, the linear electromechanical coupling in the PZE, which relates the stress and electric displacement to the strain and electric field, is given by

J. Acoust. Soc. Am. **150** (1), July 2021

André G. Steckel and Henrik Bruus   635

$$
\begin{pmatrix} \sigma_{xx} \\ \sigma_{yy} \\ \sigma_{zz} \\ \sigma_{yz} \\ \sigma_{xz} \\ \sigma_{xy} \\ D_x \\ D_y \\ D_z \end{pmatrix} = \begin{pmatrix} C_{11} & C_{12} & C_{13} & 0 & 0 & 0 & 0 & 0 & -e_{31} \\ C_{12} & C_{11} & C_{13} & 0 & 0 & 0 & 0 & 0 & -e_{31} \\ C_{13} & C_{13} & C_{33} & 0 & 0 & 0 & 0 & 0 & -e_{33} \\ 0 & 0 & 0 & C_{44} & 0 & 0 & 0 & -e_{15} & 0 \\ 0 & 0 & 0 & 0 & C_{44} & 0 & -e_{15} & 0 & 0 \\ 0 & 0 & 0 & 0 & 0 & C_{66} & 0 & 0 & 0 \\ 0 & 0 & 0 & 0 & e_{15} & 0 & \varepsilon_{11} & 0 & 0 \\ 0 & 0 & 0 & e_{15} & 0 & 0 & 0 & \varepsilon_{11} & 0 \\ e_{31} & e_{31} & e_{33} & 0 & 0 & 0 & 0 & 0 & \varepsilon_{33} \end{pmatrix} \begin{pmatrix} \partial_x u_x \\ \partial_y u_y \\ \partial_z u_z \\ \partial_y u_z + \partial_z u_y \\ \partial_x u_z + \partial_z u_x \\ \partial_x u_y + \partial_y u_x \\ -\partial_x \varphi \\ -\partial_y \varphi \\ -\partial_z \varphi \end{pmatrix}. \tag{6}
$$

The remaining three components of the stress tensor are given by the symmetry relation $\sigma_{ik} = \sigma_{ki}$. Similarly, the Cauchy equation (5) governs $\boldsymbol{u}_1$ in a purely elastic solid, but now the stress-strain relation (6) includes only the first six rows and first six columns as $\boldsymbol{D}$ and φ do not couple to $\boldsymbol{\sigma}_{sl}$ and $\boldsymbol{u}_1$. The parameter values are listed in Table SII of the supplementary material.[38]

B. Governing equations for the steady time-averaged fields

The nonlinearity of the governing equations results in higher order responses to the time-harmonic actuation. Here, we are only interested in the steady time-averaged second-order response and define $F_2(\boldsymbol{r}) = \langle \tilde{F}_2(\boldsymbol{r}, t) \rangle = (\omega/2\pi) \int_0^{2\pi/\omega} \tilde{F}_2(\boldsymbol{r}, t) \, dt$. A time-average of a product of two first-order fields is also a second-order term, which is written as $\langle \mathrm{Re}[\tilde{A}_1(t)] \mathrm{Re}[\tilde{B}_1(t)] \rangle = \frac{1}{2} \mathrm{Re}[A_1 B_1^*]$, where the asterisk denotes complex conjugation. The acoustic streaming $\boldsymbol{v}_2$ is such a time-averaged field. It is a steady-state, incompressible Stokes flow driven by the slip velocity stated in Sec. II C and time-averaged acoustic dissipation body force proportional to Γ_{fl},[37]

$$
\eta_{\mathrm{fl}} \nabla^2 \boldsymbol{v}_2 = \nabla p_2 - \frac{\Gamma_{\mathrm{fl}} \omega}{2 c_{\mathrm{fl}}^2} \mathrm{Re}[p_1^* \boldsymbol{v}_1^{\mathrm{fl}}], \quad \nabla \cdot \boldsymbol{v}_2 = 0. \tag{7}
$$

The spatial average $E_{\mathrm{ac}}^{\mathrm{fl}}$ of the time-averaged acoustic energy density in the fluid volume V_{fl} is given as the sum of the kinetic and compressional energy densities,

$$
E_{\mathrm{ac}}^{\mathrm{fl}} = \frac{1}{V_{\mathrm{fl}}} \int_{V_{\mathrm{fl}}} \left[\frac{1}{4} \rho_{\mathrm{fl}} |\boldsymbol{v}_1^{\mathrm{fl}}|^2 + \frac{1}{4} \kappa_{\mathrm{fl}} |p_1|^2 \right] dV, \tag{8}
$$

where ρ_{fl} and κ_{fl} are the fluid density and compressiblity, respectively.

The acoustic radiation force $\boldsymbol{F}^{\mathrm{rad}}$ acting on a single particle with radius a, density ρ_{ps}, and compressibility κ_{ps} suspended in the fluid is minus the gradient of the acoustic potential U^{rad},[40,41]

$$
\boldsymbol{F}^{\mathrm{rad}} = -\nabla U^{\mathrm{rad}}, \tag{9a}
$$

$$
U^{\mathrm{rad}} = \pi a^3 \left(\frac{1}{3} f_0 \, \kappa_{\mathrm{fl}} |p_1|^2 - \frac{1}{2} f_1 \, \rho_{\mathrm{fl}} |\boldsymbol{v}_1^{\mathrm{fl}}|^2 \right), \tag{9b}
$$

$$
f_0 = 1 - \frac{\kappa_{\mathrm{ps}}}{\kappa_{\mathrm{fl}}}, \quad f_1 = \frac{2(\rho_{\mathrm{ps}} - \rho_{\mathrm{fl}})}{2\rho_{\mathrm{ps}} + \rho_{\mathrm{fl}}}, \tag{9c}
$$

where f_0 and f_1 are the so-called acoustic monopole and dipole scattering coefficients, respectively.

To further quantify the quality of the acoustophoretic response in the fluid volume V_{fl} of a standing half-wave-like pressure wave, which by $\boldsymbol{F}^{\mathrm{rad}}$ focuses microparticles in the vertical nodal plane $y = 0$, we use the figure of merit R in V_{fl}, introduced by Moiseyenko and Bruus,[22]

$$
R = \frac{\int_{V_{\mathrm{fl}}} - \mathrm{sign}(y) F_y^{\mathrm{rad}} \, dV}{\int_{V_{\mathrm{fl}}} |F_z^{\mathrm{rad}}| \, dV}. \tag{10}
$$

R is large when the focusing force $-\mathrm{sign}(y) F_y^{\mathrm{rad}}$ with the appropriate sign is large and the magnitude $|F_z^{\mathrm{rad}}|$ of the vertical force is small. Essentially, R expresses how many times larger the average horizontal focusing force component is compared to the vertical focusing force component.

Another quantitative measure is the time t_{foc} it takes, on average, after turning on the acoustic field to focus by acoustophoresis a dilute suspension of microparticles of radius a into the narrow region $|y| < 8a$, centered around the vertical nodal plane $y = 0$ from their initial positions. We consider N particles that start from the evenly distributed positions $\boldsymbol{r}_i$, $i = 1, 2, \ldots, N$, outside of the narrow region. The equation of motion for a single particle with velocity $\boldsymbol{v}_{\mathrm{p}}$ suspended in a fluid with a streaming velocity $\boldsymbol{v}_2$ is the force balance between the Stokes drag force and acoustic radiation force, $\boldsymbol{v}_{\mathrm{p}}(\boldsymbol{r}) = \boldsymbol{v}_2(\boldsymbol{r}) + (1/6\pi\eta_{\mathrm{fl}}a) \boldsymbol{F}^{\mathrm{rad}}(\boldsymbol{r})$.[42] The time, t_{fi}, when a given particle reaches the narrow region, $|y_f| = 8a$, is found by numerical integration of the trajectory as detailed in the

supplementary material.[38] The average focus time for the homogeneous particle distribution is, therefore, defined by

$$t_{\text{foc}} = \frac{1}{N} \sum_{i=1}^{N} t_{fi}. \tag{11}$$

Quantitatively, for a given actuation voltage, a good acoustophoretic resonance mode is characterized by having a large E_{ac}, large R, and small t_{foc}.

C. Boundary conditions fluids, solids, and PZE

The boundary conditions of the fields on all boundaries and interfaces of the model are specified as follows. On the surfaces facing the surrounding air, we assume zero stress on the solid and PZE as well as zero free surface charge density on the PZE. On the surfaces with electrodes, the PZE has a specified alternating current (ac)-voltage amplitude. On the internal solid-PZE and solid-fluid surfaces, the stress and displacement are continuous except for the latter in the form of the effective boundary conditions derived by Bach and Bruus.[37] These boundary conditions include, analytically, the shallow viscous boundary layer of thickness $\delta_{\text{fl}} = \sqrt{2\eta_{\text{fl}}/(\rho_{\text{fl}}\omega)} \approx 0.5\,\mu\text{m}$, which, therefore, does not need to be resolved numerically, the complex-valued shear-wave number $k_s = (1+\text{i})\,\delta_{\text{fl}}^{-1}$ of the fluid (fl), and the velocity $\boldsymbol{v}_1^{\text{sl}} = -\text{i}\omega\boldsymbol{u}_1$ of the solid (sl),

$$\text{sl-air}: \quad \boldsymbol{\sigma}_{\text{sl}} \cdot \boldsymbol{n} = \boldsymbol{0}, \quad \boldsymbol{n} \text{ is the surface normal}, \tag{12a}$$

$$\text{sl-fl}: \quad \boldsymbol{\sigma}_{\text{sl}} \cdot \boldsymbol{n} = -p_1\boldsymbol{n} + \text{i}k_s\eta_{\text{fl}}\left(\boldsymbol{v}_1^{\text{sl}} - \boldsymbol{v}_1^{\text{fl}}\right), \tag{12b}$$

$$\boldsymbol{v}_1 \cdot \boldsymbol{n} = \boldsymbol{v}_{\text{sl}} \cdot \boldsymbol{n} + \frac{\text{i}}{k_s}\boldsymbol{\nabla}_{\parallel} \cdot (\boldsymbol{v}_{\text{sl}} - \boldsymbol{v}_1)_{\parallel} \tag{12c}$$

$$\text{PZE-air}: \quad \boldsymbol{D} \cdot \boldsymbol{n} = 0, \tag{12d}$$

$$\text{top elec.}: \quad \varphi = 0, \tag{12e}$$

$$\text{bot elec.}: \quad \varphi = \pm\frac{1}{2}\varphi_0. \tag{12f}$$

Further, at fluid–solid interfaces, the slip velocity $\boldsymbol{v}_2^{\text{bc}}$, driving the streaming, takes into account both the motion of the surrounding elastic solid and Reynolds stress induced in a viscous boundary layer in the fluid,[37]

$$\boldsymbol{v}_2 = \boldsymbol{v}_2^{\text{bc}}, \quad \boldsymbol{n} \cdot \boldsymbol{v}_2^{\text{bc}} = 0, \tag{13a}$$

$$(\boldsymbol{1} - \boldsymbol{n}\boldsymbol{n}) \cdot \boldsymbol{v}_2^{\text{bc}} = -\frac{1}{8\omega}\boldsymbol{\nabla}_{\parallel}|\boldsymbol{v}_{1\parallel}^{\text{fl}}|^2$$
$$- \text{Re}\left[\left(\frac{2-\text{i}}{4\omega}\boldsymbol{\nabla}_{\parallel} \cdot \boldsymbol{v}_{1\parallel}^{\text{fl}*} + \frac{\text{i}}{2\omega}\partial_{\perp}v_{1\perp}^{\text{fl}*}\right)\boldsymbol{v}_{1\parallel}^{\text{fl}}\right], \tag{13b}$$

where the subscript "$\parallel$" indicates the derivative or vector components parallel to the surface and, likewise, "$\perp$" indicates the perpendicular components. Equation (13) is the special case of the slip velocity $\boldsymbol{v}_2^{\text{bc}}$, which is only valid near the acoustic resonance, where $|\boldsymbol{v}_1^{\text{fl}}|$ in the bulk is much larger than $|\boldsymbol{v}_1^{\text{sl}}|$ of the walls at the fluid–solid interface.

Finally, we use the symmetry at the yz- and xz-planes to reduce the model to one-quarter the size in the domain $x > 0$ and $y > 0$, allowing for finer meshing and/or faster computations. We apply the symmetric boundary conditions at the yz-plane $x = 0$ and anti-symmetry at the xz-plane $y = 0$ for the first-order fields and symmetric boundary conditions at both planes for the second-order fields,

Symmetry, $x = 0$:
$$\partial_x\varphi = 0, \quad \partial_x p_1 = 0, \quad \partial_x p_2 = 0, \tag{14a}$$

$$v_{1,x}^{\text{sl}} = 0, \quad \partial_x v_{1,y}^{\text{sl}} = 0, \quad \partial_x v_{1,z}^{\text{sl}} = 0, \tag{14b}$$

$$v_{2,x}^{\text{fl}} = 0, \quad \partial_x v_{2,y}^{\text{fl}} = 0, \quad \partial_x v_{2,z}^{\text{fl}} = 0, \tag{14c}$$

Anti-symmetry, $y = 0$:
$$\varphi = 0, \quad p_1 = 0, \quad \partial_y p_2 = 0, \tag{14d}$$

$$v_{1,x}^{\text{sl}} = 0, \quad \partial_y v_{1,y}^{\text{sl}} = 0, \quad v_{1,z}^{\text{sl}} = 0, \tag{14e}$$

$$\partial_y v_{2,x}^{\text{fl}} = 0, \quad v_{2,y}^{\text{fl}} = 0, \quad \partial_y v_{2,z}^{\text{fl}} = 0. \tag{14f}$$

III. MAIN RESULTS COMPARING A THIN-FILM AND A BULK-TRANSDUCER DEVICE

A. The two main model devices

As a proof of concept that a tiny thin-film transducer is able to drive a bulk acoustofluidic device as well as a conventional bulk transducer, we study the two devices shown in Figs. 2(a) and 2(c), which both contain a water-filled microchannel of length $L_{\text{fl}} = 35\,\text{mm}$, width $W_{\text{fl}} = 0.377\,\text{mm}$, and height $H_{\text{fl}} = 0.157\,\text{mm}$, chosen as a typical channel size used in the literature[1] and specifically studied experimentally and theoretical in Ref. 43. We emphasize that both devices are simulated on equal footing using the same model approach with the same assumptions on damping and lack of clamping. Also, both devices are made of acoustically hard materials with high acoustic impedances relative to water, namely, 13.2 for silicon and 8.4 for glass.

The thin-film device consists of a rectangular glass block of $L_{\text{gl}} = 40\,\text{mm}$, width $W_{\text{gl}} = 3.02\,\text{mm}$, and height $H_{\text{gl}} = 1.4\,\text{mm}$. An $\text{Al}_{0.6}\text{Sc}_{0.4}\text{N}$ thin-film transducer of length $L_{\text{thf}} = L_{\text{gl}}$, width $W_{\text{thf}} = W_{\text{gl}}$, and height $H_{\text{thf}} = 1\,\mu\text{m}$ is deposited on the bottom surface of the xy-plane, thus, occupying only 0.07% of the total device volume. To excite the half-wave-like pressure wave, an antisymmetric voltage actuation is effective[23] and made possible by splitting the bottom electrode in half by a 40-μm-wide gap along the x axis. The microchannel is centered along the x- and y axes, but its top aligns with the center of the glass height $\frac{1}{2}H_{\text{gl}}$ to mimic that the glass block consists of two glass slabs of equal height bonded together except that the microchannel is etched into the top surface of the bottom slab; see Fig. 1. This specific device is chosen because in a recent study, we successfully modeled and experimentally validated a similar thin-film-glass-block device without the microchannel.[44]

J. Acoust. Soc. Am. **150** (1), July 2021

André G. Steckel and Henrik Bruus   637
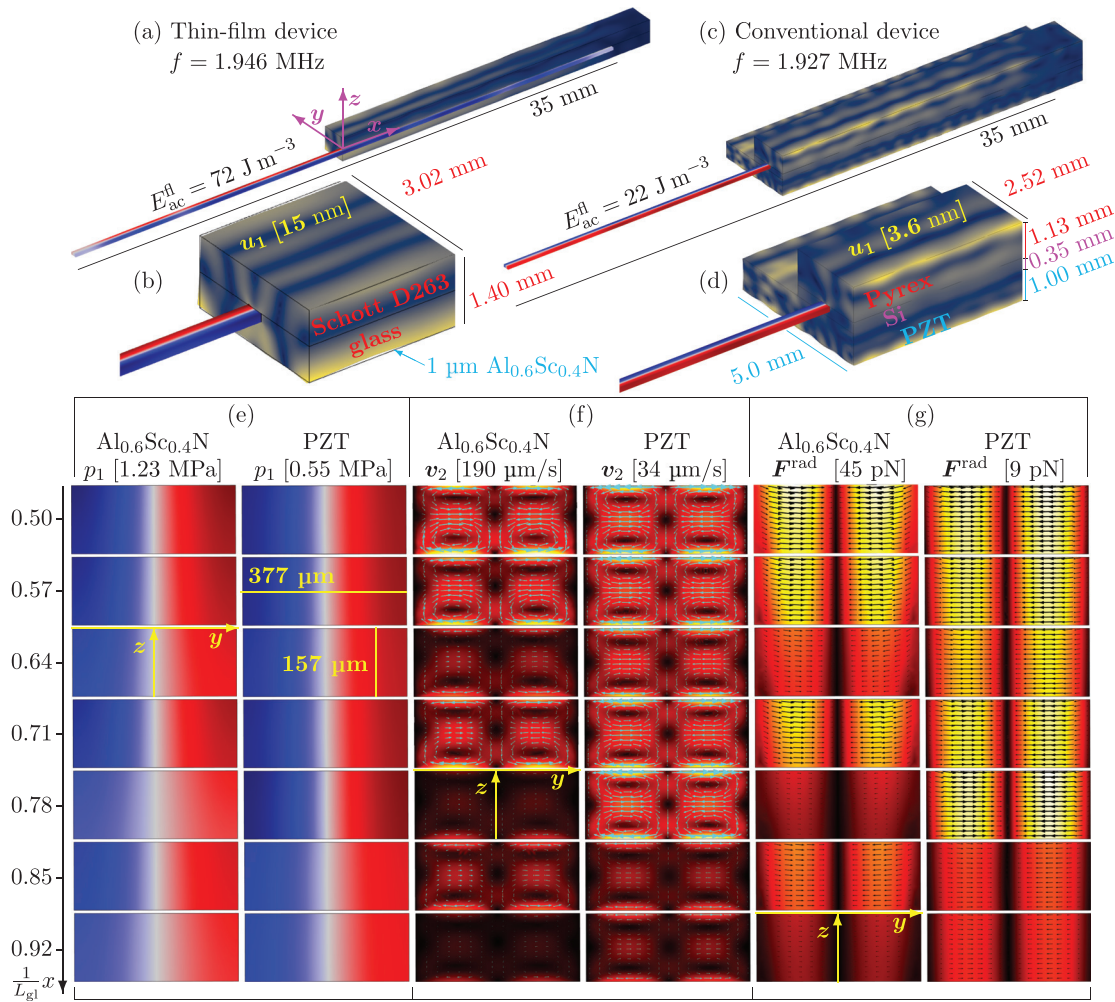
FIG. 2. (Color online) (a),(b) A bulk glass chip driven by a 1-μm-thick Al$_{0.6}$Sc$_{0.4}$N thin-film transducer (not visible) actuated at resonance $f = 1.946$ MHz with 1 V$_{pp}$. The 3D color plots are u_1 from 0 (blue) to 15 nm (yellow) and p_1 from -1.23 MPa (blue) to $+1.23$ MPa (red). (c),(d) A conventional Si-glass chip driven by a bulk PZT actuated at resonance $f = 1.927$ MHz with 1 V$_{pp}$. The color plots are u_1 from 0 (blue) to 3.6 nm (yellow) and p_1 from -0.55 MPa (blue) to $+0.55$ MPa (red). (e) The color plots of p_1 from $-p_{max}$ (blue, value in the square bracket) to $+p_{max}$ (red) of the Al$_{0.6}$Sc$_{0.4}$N-driven device on the left and PZT-driven device on the right in seven cross sections from $x/L_{gl} = 0.5$ to 0.92 in steps of 0.07 are shown. (f) The color plots as in (e) but for the streaming velocity magnitude v_2 from zero (black) to v_2^{max} (white, value in the square bracket) and with vectors showing v_2. (g) The color and vector plot as in (f) but for the radiation force F^{rad} from zero (black) to F^{rad}_{max} (white, value in the square bracket) for suspended 5-μm-diameter polystyrene particles. See the animations of the modes in the supplementary material (Ref. 38).

The bulk-transducer device has been studied extensively both experimentally and numerically in the literature.[36,42,43] It consists of a silicon substrate of length $L_{sl} = 40$ mm, width $W_{sl} = 2.52$ mm, and height $H_{si} = 0.35$ mm into which the centered microchannel is etched and onto which is bonded a Pyrex glass lid of the same length and width but with the height $H_{py} = 1.13$ mm. This silicon-glass chip is placed off-center on a nominal 2-MHz PZT transducer of $L_{pzt} = 40$ mm, width $W_{pzt} = 5$ mm, and height $H_{pzt} = 1$ mm such that the rightmost side walls align. In the actual device, the transducer is glued to the chip, but here we neglect the glue layer and assume an ideal bonding instead. Note that the fraction of the total volume occupied by the bulk-PZT transducer is large, $\mathcal{V}_{pzt}/\mathcal{V}_{tot} = 57\%$ v/v.

Using these dimensions and the material parameters listed in Tables SI and SII of the supplementary material,[38] we implement these two 3D device models in the commercial finite-element software COMSOL Multiphysics 5.4,[45] closely following the implementation method described in Ref. 34. We use tetrahedral meshes chosen to have at least 12 nodal points per wavelength at 2 MHz in all domains (18 in the fluid domain) except in the z-direction of the thin-film, where the thickness is much smaller than the wavelength. So here, a swept mesh was used to ensure at least four nodal points. Performing a standard mesh convergence analysis,[34] we found deviations in the acoustofluidic responses of about 1% when comparing to the highest mesh resolution possible in our setup. We observed no changes by adding additional nodal points in the thin-film thickness direction. All simulations were run on a workstation with a 16-core processor Intel i9-7960X at 3.70 GHz boost clock and 128 GB random access memory (Intel, Santa Clara, CA).

B. Mode analysis of the two devices

The first step in our analysis is to identify good acoustic resonance modes in the two devices, which we actuate in a

comparable manner with a peak-to-peak voltage of $\varphi_0 = 1$ V. In the thin-film device, the voltage amplitude of the ac-voltage on the "positive" ("negative") half of the bottom electrode is set to $+\frac{1}{2}\varphi_0$ ($-\frac{1}{2}\varphi_0$, 180° out of phase) relative to the grounded top electrode. Similarly, the voltage amplitude on the top electrode in the bulk-PZT device is set to $+\frac{1}{2}\varphi_0$ relative to the grounded bottom electrode. The frequency of the actuation voltage is then swept from 0.1 to 3.5 MHz while monitoring the acoustic energy density E_{ac}^{fl}, Eq. (8), in the water. The frequency steps in the sweep are adaptive, ranging from $\Delta f = 16$ kHz when the local curvature in $E_{ac}^{fl}(f)$ is small (far from resonance peaks) down to $\Delta f = 0.03$ kHz when it is large (near resonance peaks).

As expected, the strongest resonance peak in E_{ac}^{fl} happens near the hard-wall standing half-wave resonance $f_0 = c_{fl}/2W_{wa} = 2$ MHz. This main resonance is located at $f_{thf} = 1.946$ MHz with a maximum energy density of $E_{ac}^{fl}(f_{thf}) = 72$ J m^{-3} for the thin-film device and at $f_{pzt} = 1.927$ MHz with a $E_{ac}^{fl}(f_{pzt}) = 22$ J m^{-3}. The amplitude p_1 of the pressure and $\boldsymbol{u}_1$ of the displacement field for these main resonance modes in the two devices are shown in Figs. 2(a)–2(d). One immediate conclusion is that the quality of the resulting resonant pressure mode in the two devices is comparable: a nearly perfect antisymmetric wave across the channel with only weak variations along the channel. The pressure amplitude of 1.23 MPa in the thin-film device is 2.2 times larger than the 0.55-MPa amplitude in the bulk-PZT device.

When inspecting the displacement field in Figs. 2(a)–2(d), it is seen that it has a more regular mode with a larger 15-nm amplitude in the thin-film device [Figs. 2(a) and 2(b)]compared to the more complex resonance mode with a smaller 3.6-nm amplitude in the larger volume of the bulk-PZT device [Figs. 2(c) and 2(d)]. Figure 2(e) shows the pressure in seven vertical channel –cross sections, equally spaced along the channel from its center to its end, showing the abovementioned weak axial variations in p_1 for both devices. Clearly on a qualitative level, the tiny 0.07% v/v thin-film transducer is seen to deliver a comparable, and perhaps even better, acoustic response in the device compared with the conventional large 57% v/v bulk-PZT transducer.

As a first rough quantitative comparison, we sample p_1 in 700 equidistant points along a straight line parallel to the x axis through the edge point $\left(0, \frac{1}{2}W_{fl}, -\frac{1}{2}H_{fl}\right)$. We find the following regression lines with standard deviations: $p_1\left(x, \frac{1}{2}W_{fl}, -\frac{1}{2}H_{fl}\right) = \left(1.15 - 0.83\frac{2x}{L_{fl}} \pm 0.16\right)$ MPa for the thin-film and $(0.56 - 0.23(2x/L_{fl}) \pm 0.05)$ MPa for the bulk-PZT device. The former pressure is nearly twice as large as the latter at the center $x = 0$, namely, 1.15 versus 0.56 MPa, but they both end at the same value at the channel end $x = \frac{1}{2}L_{fl}$, namely, 0.32 versus 0.33 MPa. Clearly, the pressure is higher in the thin-film device, but the pressure variations are also three times larger, namely, 0.16 versus 0.05 MPa compared to the bulk-PZT device. In the following, for further quantitative comparison, we study the acoustic radiation force $\boldsymbol{F}^{rad}$ and related focusing time t_{foc} that it takes to focus 5-μm-diameter particles in the vertical pressure nodal plane $y = 0$.

C. The acoustic radiation force and streaming at resonance

The acoustic modes p_1 and $\boldsymbol{u}_1$ are the basic fields giving rise to the steady time-averaged responses used for applications in acoustofluidic devices, namely, the acoustic streaming $\boldsymbol{v}_2$ in the fluid and the radiation force $\boldsymbol{F}^{rad}$ acting on the suspended microparticles. In Figs. 2(f) and 2(g), these responses are shown in the same seven cross sections as were used in Fig. 2(e). Being second-order responses, the amplitudes of $\boldsymbol{v}_2$ and $\boldsymbol{F}^{rad}$ become $2.2^2 \approx 5$ larger in the thin-film than in the bulk-PZT device, where 2.2 is the aforementioned ratio in the pressure amplitudes. Similarly, the axial variations in $\boldsymbol{v}_2$ and $\boldsymbol{F}^{rad}$ are nearly five times larger in the thin-film than they are in the bulk-PZT device.

For a more complete quantitative comparison of the acoustophoretic response, we compute the acoustic energy density E_{ac} [Eq. (8)], the figure of merit R [Eq. (10)], and the focusing time t_{foc} [Eq. (11)] for suspended 5-μm-diameter microparticles for the two main resonance modes in Fig. 2. As detailed in the supplementary material,[38] t_{foc} for a given mode is given by the average of the focus time of 3536 individual particle trajectories computed by numerical integration. The respective values are listed in Table I, and they support the result of the qualitative comparison of the shape of the pressure, streaming, and force fields: The time-averaged response of the Al$_{0.6}$Sc$_{0.4}$N thin-film device is comparable in terms of E_{ac}, R, and t_{foc} to that of the bulk-PZT device. It supports the usual quadrupolar Rayleigh streaming pattern, and the radiation force points toward the vertical center plane along the axis, which can, thus, serve as a plane for particle focusing. Whereas R is 22.7/7.1 = 3.2 times smaller, E_{ac}^{fl} is 72/22 = 3.3 times larger and t_{foc} is 1.73/0.53 = 3.3 times faster in the thin-film device compared to the bulk-PZT device. From this first example, it is, therefore, clear that the thin-film bulk device would work as an excellent acoustofluidic device and thin-film transducers can be used on generic bulk chips without fabricating the

TABLE I. The quantitative comparison of the quality of the resonance modes of three thin-film (thf) and one bulk (bulk) device: Al$_{0.6}$Sc$_{0.4}$N (thf) and Pz26 (bulk) of Fig. 2, as well as AlN (thf) and Pz26 (thf) discussed in Sec. IV B. Listed are the resonance frequency f_{res}, the figure of merit, Eq. (10), the acoustic energy density E_{ac}, Eq. (8), and the focusing time t_{foc}, Eq. (11), for 5-μm-diameter microparticles. See the animations of the resonance modes in the supplementary material (Ref. 38).

Response	AlN thf	Al$_{0.6}$Sc$_{0.4}$N thf	Pz26 thf	Pz26 bulk
f_{res} (MHz)	1.948	1.946	1.942	1.927
R (-)	6.7	7.1	8.5	22.7
E_{ac}^{fl} (J m^{-3})	7.3	72	2.1×10^3	22
t_{foc} (s)	5.4	0.52	0.016	1.73
$E_{ac}^{fl} t_{foc}$ (J s m^{-3})	39.4	37.4	34.2	38.1
$E_{ac}^{fl}/e_{31,f}^2$ (m F^{-1}; Ref. 38)	7.0	10.3	9.9	—

J. Acoust. Soc. Am. **150** (1), July 2021

André G. Steckel and Henrik Bruus   639

delicate and expensive membrane devices.[21] In the following, we investigate further the physical characteristics of the thin-film bulk device.

IV. PHYSICAL ASPECTS OF ACOUSTOFLUIDIC BULK DEVICES DRIVEN BY THIN-FILM TRANSDUCERS

In this section, we use the numerical model to study various physical aspects of acoustofluidic devices with thin-film transducers. The study includes the physical principle of the thin-film transduction process; the robustness of the device to the material, thickness, and quality factor of the thin-film transducer; the role of the thin-film-transducer electrode shape; the spatial regularity; and the sensitivity of the device to shifts in the channel position away from the exact centering in the glass chip.

A. The physics of thin-film actuation of bulk devices

The ability of the thin-film transducer to create the desired acoustophoretic microparticle focusing by radiation force or mixing by acoustic streaming in a bulk acoustofluidic device relies on three physical aspects of the system: the in-plane-expansion of the thin-film transducer under the action of the orthogonal applied electric field, the acoustic whole-system resonance of the device, and the high Q-factor of the elastic solid, constituting the bulk part of the device.

Traditional bulk PZE transducers typically work by exciting a standing half-wave in the transducer thickness direction, which is also the direction of both the polarization and applied electrical field. This gives a large mechanical displacement because of the large longitudinal PZE coefficient e_{33}. This thickness mode is fairly easy to compute and design for, and it is also relatively good at transferring acoustical power into a device attached to the transducer by the large displacement component along the surface normal. Conventional bulk PZE transducers with a millimeter-thickness typically have good resonances in the low-MHz regime.

In contrast, the half-wave transducer resonances of the thin-film transducers are pushed up into the GHz regime as a result of the micrometer-sized thickness, which is much higher than the low-MHz frequencies typically used in bulk acoustofluidics. Therefore, the transduction studied in this work is dominated by the transverse PZE coefficient $e_{31,f}$. The large electric field on the order of MV/m that results from applying, say, a potential difference of 1 V_{pp} across a 1-μm-thick thin-film transducer, generates a large strain that accumulates along the millimeter-sized transducer–glass interface, which is the first of the three physical prerequisites. When this strain pattern has a sufficiently compatible overlap with that of a given resonance mode in the large glass block, the system will be excited at a frequency near this resonance mode frequency. This is the second physical prerequisite. We emphasize that this transduction mechanism does not rely on exciting any resonances in the thin-film transducer but instead on exciting resonances in the whole system, of which the transducer is only a minute part.
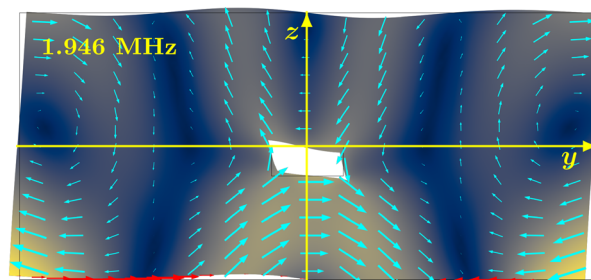
FIG. 3. (Color online) The 3D numerical simulation in the yz-plane at $x=0$ of the displacement field $\boldsymbol{u}_1$ (enhanced by a factor of 7000 for clarity) in the $Al_{0.6}Sc_{0.4}N$ thin-film device of Fig. 2(a) at the whole-system resonance $f_{thf} = 1.946$ MHz. The vector plot of $\boldsymbol{u}_1$ (cyan vectors) and color plot of its magnitude u_1 from 0 (dark blue) to 15 nm (light yellow) is shown. The mode is excited by the $Al_{0.6}Sc_{0.4}N$ thin-film transducer driven by a 1-V_{pp} ac-voltage at the frequency $f = 1.946$ MHz. The in-plane strain $\partial_y u_{1,y}\, \boldsymbol{e}_y$ (red vectors) generated by the transducer on the transducer-glass interface shows expansion on the left and contraction on the right side in a way that is compatible with the strain field of the whole-system resonance mode. See the animations of the modes in the supplementary material (Ref. 38).

The thin-film transduction mechanism is exemplified in Fig. 3 (and in the corresponding animation in the supplementary material[38]) by the mode f_{thf} in the thin-film device [Fig. 2(a)]. The in-plane strain $(\partial_y u_{1,y})\boldsymbol{e}_y$ on the transducer–glass interface generated by the antisymmetrically driven split-bottom-electrode thin-film transducer corresponds to an expansion on the left side and a contraction on the right side. This strain pattern is compatible with that of the whole-system resonance mode, which, therefore, is excited with a large 15-nm displacement amplitude. The resulting antisymmetric oscillatory displacement field of the glass block pushes on the water in the channel, which leads to an antisymmetric pressure wave p_1 [Fig. 2(e)] with the desired acoustofluidic properties shown in Figs. 2(f) and 2(g).

The third and last physical prerequisite is the high-quality factor of the whole system as an acoustic resonator. Because the thin-film transducer in our main example constitutes only a 0.07% v/v, the quality factor is completely dominated by that of the glass block, which has a high value, $Q \sim 10^3$, in a typical glass.[39]

B. The robustness of the device to the material, thickness, and quality factor of the thin-film transducer

The above thin-film transduction method implies that the functionality of the thin-film acoustofluidic device is robust to changes in several characteristic properties of the thin-film transducer, essentially because of its small volume fraction of the whole system. In the following, we study three such properties, namely, the material, thickness, and quality factor of the thin-film transducer.

We simulate three types of PZE materials. One is the commonly used PZT, having large PZE coefficients. One drawback of this material is its lead content, which is being out-phased for health and environmental reasons, and another is the difficulty in fabricating the material with a sufficiently low dissipation. Whereas other materials have

lower PZE coefficients than PZT, they may be fabricated with higher purity and less dissipation. The lead-free AlN is a choice for its simpler and better well-controlled high-quality depositing on a variety of substrates, which allows for higher break-down voltages that may compensate for the lower PZE coefficient. $Al_{1-x}Sc_xN$ offers a PZE coefficient between the values of PZT and AlN with many of the same advantages as AlN, but it has a more complex fabrication process and alower break-down voltage.

In the first three columns of Table I, the simulation results of these different PZE materials are listed, while keeping all other quantities fixed in the model: AlN, $Al_{0.6}Sc_{0.4}N$, and PZT Pz26, and maintaining this order when referring to the numerical results in the following. In spite of the very different material parameters listed in Table SII of the supplemental material,[38] the resulting acoustofluidic response of the main resonance f_{thf} is nearly the same shapewise, and only the amplitudes vary. Within 0.3%, the resonance frequencies are identical, $f_{thf} = 1.948$, 1.946, and 1.942 Mz, whereas the field amplitudes reflect the difference in the PZE coefficients and are for the pressure $|p_1| = 0.44$, 1.20, and 3.50 MPa, the displacement $|u_1| = 5.1$, 15, and 38 nm, and the acoustic energy density $E_{ac}^{fl} = 7.3$, 72, and 2.1×10^3 J m^{-3}. Besides the obvious difference in the amplitude, the computed whole-system resonance is nearly the same in all three cases, showing a nearly ideal antisymmetric pressure wave in the microchannel. This is also reflected in the last two rows of Table I, which show how well the scaling laws $t_{foc}^{-1} \propto E_{ac}^{fl} \propto e_{31f}^2$ are obeyed in the three cases.

The thin-film device is also insensitive to the quality factor of the thin-film transducer, which, in terms of the damping coefficient Γ_{sl} in the Cauchy equation (5), is given by $Q = \frac{1}{2}\Gamma_{sl}^{-1}$. For two reasons, we expect a weak dependency on Q. The tiny volume of the transducer implies that the Q-factor of the system is completely dominated by that of the glass block. Consequently, as the transduction mechanism does not rely on the resonance properties of the thin-film transducer, the strong Q-dependence that is usually associated with the resonant modes in the transducer is absent. The simulation results shown in Fig. 4 confirm this expectation. Here, the acoustic energy density E_{ac}^{fl} in the microchannel of the thin-film device [Fig. 2(a)] at the resonance $f_{thf} = 1.946$ MHz is shown as a function of Q from the original value of 1000 down to an appalling low value of 5. The resonant behavior reflected in $E_{ac}^{fl}(f)$ is maintained, and the change in Q by a factor of 200 results in a drop of the peak value of E_{ac}^{fl} by a factor of only 2, from 72 to 40 J m^{-3}.

Finally, the simulation results in Fig. 4 also show that the main resonance mode f_{thf} is maintained when changing the thickness by a factor of 3.5 from $H_{thf} = 1$ to 3.5 μm, numbers typical for the current AlN and $Al_{1-x}Sc_xN$ thinfilm fabrication technology. The amplitude of the resonance peak in E_{ac}^{fl} is nearly constant (72 ± 1) J m^{-3} from the thinnest to thickest film.
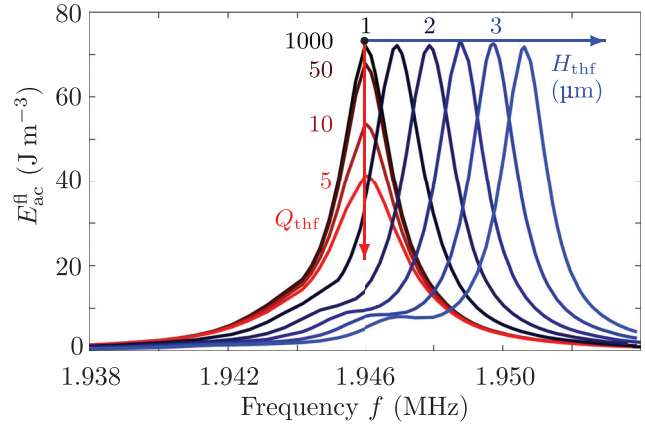
FIG. 4. (Color online) The 3D simulations of the acoustic energy density E_{ac}^{fl} of the resonance mode for the system shown in Fig. 2(a) versus the frequency from 1.938 to 1.954 MHz as a function of the thin-film Q-factor Q_{thf}, decreasing from 1000, 50, and 10 to 5 (red arrow), and as a function of the thin-film thickness H_{thf}, increasing from 1 to 3.5 μm in steps of 0.5 μm (blue arrow).

C. Enhancing the acoustic response of the device by shaping the electrodes of the thin-film transducer

Thin-film transducers are fabricated by standard microfabrication deposition techniques, and this implies several distinct advantages. The lateral shape of the transducer or its electrode can be chosen freely by photolithography techniques; the attachment of the transducer to the glass chip is reproducible, stable, and strong, and the less controlled use of glue, known from standard bulk-transducer technology,[46] is avoided. Commercially, microfabrication techniques open up for volume production with relatively cheap unit prices, a necessary prerequisite for widespread single-use applications in biotechnology and medicine, where the crosscontamination arising from the multiple use of the same device is a no go.

An illustrative example of how the shape of the metal electrodes on the surface of the thin-film transducer may enhance the acoustic response is shown in Fig. 5. Here, the thin-film device of Fig. 2(a) is used as a starting point, but instead of the split-bottom electrode used for antisymmetric excitations, the bottom electrode is used for symmetric excitations in the three different cases of Figs. 5(a)–5(c), keeping all other parameters fixed: (a) an un-split electrode, (b) a large-gap split electrode, and (c) a two-gap split electrode. The aim is to excite with varying strength the symmetric full-wavelength-like pressure mode having two vertical nodal planes, which obeys the symmetry condition $p_1(x, -y, z) = p_1(x, y, z)$. Indeed, such a symmetric whole-system resonance is located at $f = 3.578$ MHz as shown in Figs. 5(d)–5(g). As listed in Fig. 5(h), the strength of the mode depends on the electrode design. By reducing the electrode coverage from 100% in case (a) to 33% in case (b), the acoustic energy can be increased by a factor of 2. Another factor of 2 is obtained by having the 49% electrode coverage of case (c), which includes an excitation voltage of $+\varphi_0$ on the outer electrodes and $-\varphi_0$ on the center electrode.
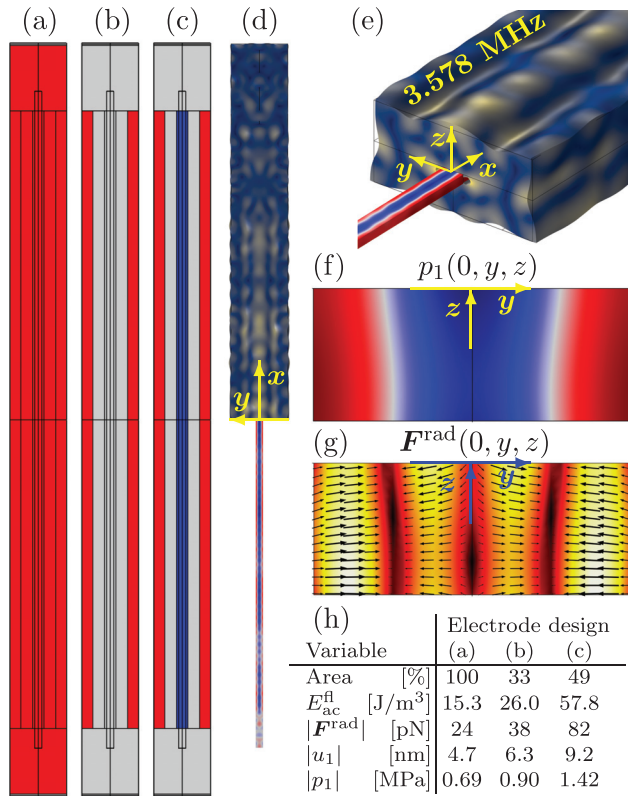
FIG. 5. (Color online) Simulations of the device in Fig. 2(a) but now exciting the symmetric full-wave-like resonance mode at $f = 3.578$ MHz. [(a)–(c)] Three designs of a symmetric bottom electrode for exciting this mode, where red is actuated by $\varphi = +\varphi_0$, blue is actuated by $\varphi = -\varphi_0$, and gray marks no electrode. The top electrode is grounded, $\varphi = 0$. [(d)–(g)] The 3D simulations of $\boldsymbol{u}_1$, p_1, and $\boldsymbol{F}^{\mathrm{rad}}$ in the device with electrode design (c) using the same plot format as in Fig. 2 but with the color scales given in (h), together with the acoustic energy density E_{ac} and the area (in %) covered by the bottom electrode for all three electrode designs. See the supplementary material for animations of the resonance mode in all three cases (Ref. 38).

The explanation of this result is found in the spatial form of the whole-system resonance mode. By inspection, we see that the displacement field at the glass-transducer interface forms a wave with in-plane contractions and expansions. The PZE coefficient e_{31f} in the transducer implies the presence of an electric field with a vertical component that changes sign along the in-plane direction. This tendency is counteracted by the fully covering bottom electrode, which imposes a unidirectional electrical field. Consequently, by removing the central part of the bottom electrode (or adding the anti-phase central part), this constraining boundary condition is relaxed (or changed into a supporting condition) while the remaining side parts of the electrode are still capable of exciting the whole-system resonance mode. This example offers a glimpse of the opportunities for design improvements by performing a shape optimization of the electrodes or perhaps the entire thin-film transducer.

D. Spatially regular modes in the thin-film device

Intuitively, the simplicity of the thin-film device consisting essentially of just a glass block should lead to simpler

modes with regular spatial dependencies. As mentioned above, the presence of a bulky PZT transducer leads to the excitation of whole-system resonance modes with a more irregular wave pattern in the displacement fields. Also, experimentally, this has been observed as hot spots in the pressure field along an otherwise perfectly shaped rectangular microchannel.[36]

In Fig. 6(a), we show six different whole-system resonance modes at lower frequencies near 1 MHz in a thin-film device with a 1-μm-thick split-bottom-electrode AlN thin-film transducer mounted on the bottom of a rectangular Schott D263 glass block (Schott Suisse SA, Yverdon, Switzerland) of length $L_{\mathrm{sl}} = 45$ mm, width $W_{\mathrm{sl}} = 2.8$ mm, and height $H_{\mathrm{sl}} = 1.4$ mm. The microchannel of the system has length $L_{\mathrm{fl}} = 40$ mm, width (at its top) $W_{\mathrm{fl}} = 0.43$ mm, and height $H_{\mathrm{fl}} = 0.15$ mm. To mimic the shape obtained by the isotropic etching in the glass, the side walls are modeled as quarter circles as shown in Fig. 6(b). The quarter circles increase the resonance frequency, but by increasing the channel width, we maintain a usual half-wave-like resonance mode close to 2 MHz as in Fig. 2(a). The frequencies of the resonance modes near 1 MHz are far from this 2 MHz and, thus, we would not expect these modes to be very strong. However, a clear spectrum with well-separated resonance
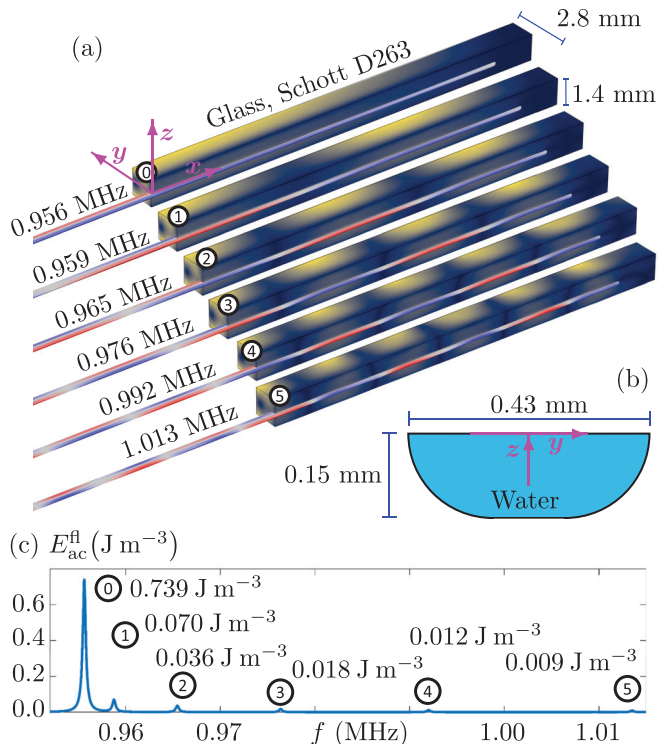
FIG. 6. (Color online) The simulation of the low-frequency modes near 1 MHz in a thin-film device with a 1-μm-thick split-bottom-electrode AlN thin-film transducer. The system is symmetric around the vertical center plane at $x = 0$ and antisymmetric around the vertical center plane at $y = 0$. (a) The lowest six resonance modes $n = 0, 1, \ldots, 5$ with $2n$ nodal planes along the x axis and one nodal plane along the y axis. The plot format is the same as in Fig. 2(a). (b) The cross-sectional shape of the microchannel in the vertical yz-plane. (c) The acoustic energy density spectrum $E_{\mathrm{ac}}^{\mathrm{fl}}(f)$ identifying the six resonance modes. See the supplementary material for animations of the six resonance modes (Ref. 38).

modes appears as shown in Fig. 6(c), yet another example of whole-system resonances excited by the thin-film transducer.

The antisymmetric actuation of the split-bottom electrode, combined with the geometrical symmetry, dictates that the system is symmetric around the vertical plane, at $x = 0$, across the device, and antisymmetric around the vertical plane, at $y = 0$, along the device. In Fig. 6(a), one immediately notices the spatial regularity of both the displacement field $\boldsymbol{u}_1$ and pressure field p_1 in the six displayed modes. Both fields have the required symmetry along the x axis and anti-symmetry along the y axis, and both fields exhibit one nodal plane along the transverse y direction and, respectively, $2n$ nodal planes with $n = 0, 1, 2, \ldots, 5$ along the axial x direction. In Fig. 6(c), the spectrum $E_{\mathrm{ac}}^{\mathrm{fl}}(f)$ in the frequency range from 0.952 to 1.015 MHz is shown, which allows for the identification of the six resonance frequencies $f_{n,1,0}$, where the indices refer to the number of nodal planes in each direction. Of the six modes, the $n = 0$-mode without nodes along the x axis has an axial structure that matches the x-independent voltage boundary condition better than the other modes, and indeed it has the highest energy density. As the number n of x axis nodes increases, the corresponding mode exhibits an increasing number of nodes and, hence, an increasing mismatch with the x-independent voltage boundary condition. This explains the monotonically decreasing peak value of $E_{\mathrm{ac}}^{\mathrm{fl}}$ for the increasing values of n shown in Fig. 6(b).

E. Device sensitivity to breaking of geometrical symmetries

As a final point, we discuss the consequences of breaking the perfect anti-symmetry of the thin-film device imposed in Figs. 2, 3, and 6. Using the microfabrication techniques, many geometrical features can be defined with accuracies down between 1 and 10 μm; however, it can be problematic to reach such accuracies when dicing up a full-sized wafer into the individual devices. For microelectronics, this is not problematic if the integrated circuits are sufficiently removed from the edges. However, for acoustofluidic devices, the whole substrate influences the whole-system resonances. For this reason, it is interesting to investigate the sensitivity of a given acoustofluidic device given shifts in the position of the microchannel relative to the edges of the substrate.

In Fig. 7, we study the acoustic response to a shift in the center axis of the microchannel in the thin-film device of Fig. 2(a) from the ideal symmetric position at $y = 0$ to 50 and 100 μm. The whole-system-resonance mode is not degraded significantly by this shift, which adds to the robustness in the experimental applications. A contributing factor to this robustness is that the water-filled channel only constitutes 1.2% of the total volume of the device. We notice that the main antisymmetric form of the acoustic pressure is largely unaffected by the shift, and the acoustic energy density $E_{\mathrm{ac}}^{\mathrm{fl}}$ remains high in the range from 55 to 78 J m^{-3}. However, as the shift increases, more pronounced axial inhomogeneities develop. Such inhomogeneities may imply a degradation in the functionality for stop-flow applications; however, as is well known experimentally from the measurements on several acoustofluidic devices in flow-through applications, such axial inhomogeneities averages out, and the device would work essentially without degradation.[20]

V. CONCLUSION AND OUTLOOK

In this paper, based on a well-tested and experimentally validated numerical model,[23,34,35] we have shown by 3D numerical simulations in Sec. III, including Fig. 2 and Table I, that bulk glass chips with integrated PZE thin-film transducers constituting less than 0.1% v/v of the device have an acoustofluidic response on par with that obtained in a conventional silicon-glass device actuated by a PZT transducer, quantified by $E_{\mathrm{ac}}^{\mathrm{fl}}$, R, and t_{foc}. The analysis in Sec. IV A demonstrated that the ability of the thin-film transducer to induce the desired acoustofluidic response in a bulk device relies on three physical aspects of the system: the in-plane-expansion of the thin-film transducer under the action of the orthogonal applied electric field, the acoustic whole-system resonances of the device, and the high Q-factor of the elastic solid, constituting the bulk part of the device.

We have pointed out some of the advantages of using thin-film transducers. Among them is the low sensitivity of the thin-film device to the material, thickness, and quality

(a) $E_{\mathrm{ac}}^{\mathrm{fl}} = 72$ J m^{-3} $p_1 = 1.23$ MPa   0 μm channel off-set ↑   1.946 MHz $u_1 = 15$ nm

(b) $E_{\mathrm{ac}}^{\mathrm{fl}} = 78$ J m^{-3} $p_1 = 1.70$ MPa   50 μm channel off-set ↑   1.954 MHz $u_1 = 22$ nm

(c) $E_{\mathrm{ac}}^{\mathrm{fl}} = 55$ J m^{-3} $p_1 = 1.44$ MPa   100 μm channel off-set ↑   1.955 MHz $u_1 = 29$ nm
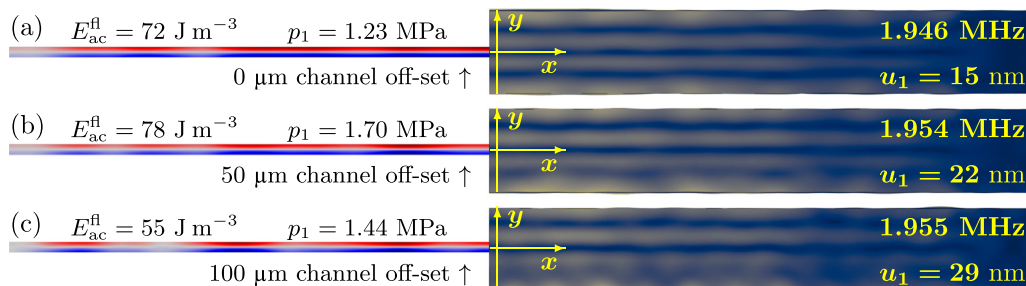
FIG. 7. (Color online) (a) The resonance mode at $f = 1.946$ MHz of the device shown in Fig. 2(a), and using the same plot format, with the acoustic energy density $E_{\mathrm{ac}} = 72$ J m^{-3} and maximum pressure amplitude $p_1 = \pm 1.23$ MPa in the fluid, and maximum displacement amplitude $u_1 = 15$ nm in the solid. (b) The same as that in (a) but with the channel offset 50 μm in the y direction and with resonance frequency $f = 1.954$ MHz, $E_{\mathrm{ac}} = 78$ J m^{-3}, $p_1 = \pm 1.70$ MPa, and $u_1 = 22$ nm. (c) The same as that in (a) but with the channel offset by 100 μm in the y direction and with resonance frequency $f = 1.955$ MHz, $E_{\mathrm{ac}} = 55$ J m^{-3}, $p_1 = \pm 1.44$ MPa, and $u_1 = 29$ nm. See the supplementary material for animations of the three resonance modes (Ref. 38).

J. Acoust. Soc. Am. **150** (1), July 2021

André G. Steckel and Henrik Bruus   643

factor of the thin-film transducer discussed in Sec. IV B. Another advantage is that thin-film devices can be produced by clean-room microfabrication techniques, similar to the ones employed in the fabrication of surface acoustic waves. These techniques make it possible to shape the transducer electrodes, and in Sec. IV C, we discussed how to exploit this design freedom to boost the acoustofluidic response in the example of Fig. 5 by a factor of 4 by carefully shaping the transducer electrodes and reducing their area. We have also exploited the advantage of the microfabrication techniques that the thin-film transducers are integrated in the devices without involving the use of glue or glycerol coupling layers, which are used in the conventional bulk-transducer technique, although they are hard to control and often result in diminished reproducibility.

The performance of the thin-film and bulk-PZT bulk devices have been compared on equal footing using the same model approach and the same assumptions on damping and lack of clamping. More accurate simulation predictions for both types of devices would require better knowledge of the material parameters, the actual damping mechanisms in all elements of the devices, and modeling of the specific clamping and tubing of the device to the measurement setup. The influence of these factors on the functionality of especially the thin-film device will be part of future studies in close collaboration with experimental colleagues.

In an application perspective, the use of thin-film transducers offers new possibilities in the field of acoustofluidics. The fact that the thin-film transducer constitutes such a low volume fraction implies not only that the device is relatively insensitive to the quality of the thin film but also that the core part of the acoustofluidic system, namely, the microchannel, constitutes a relatively larger part of the system and is, thus, easier to control. The AlN-based thin-film transducers can be fabricated with high breakdown voltages ($\sim$20 V/μm), which more than compensates for its lower coupling coefficient e_{31f}, and lower the dissipation and heat production.

We hope that this theoretical analysis will inspire our experimental colleagues in the field to investigate the new application aspects offered by the thin-film acoustofluidic devices.

ACKNOWLEDGMENTS

[1] A. Lenshof, C. Magnusson, and T. Laurell, "Acoustofluidics 8: Applications in acoustophoresis in continuous flow microsystems," Lab Chip **12**, 1210–1223 (2012).

[2] M. Gedge and M. Hill, "Acoustofluidics 17: Surface acoustic wave devices for particle manipulation," Lab Chip **12**, 2998–3007 (2012).

[3] E. K. Sackmann, A. L. Fulton, and D. J. Beebe, "The present and future role of microfluidics in biomedical research," Nature **507**(7491), 181–189 (2014).

[4] T. Laurell and A. Lenshof, eds., *Microscale Acoustofluidics* (Royal Society of Chemistry, Cambridge, UK, 2015).

[5] M. Antfolk and T. Laurell, "Continuous flow microfluidic separation and processing of rare cells and bioparticles found in blood—A review," Anal. Chim. Acta **965**, 9–35 (2017).

[6] P. Ohlsson, M. Evander, K. Petersson, L. Mellhammar, A. Lehmusvuori, U. Karhunen, M. Soikkeli, T. Seppa, E. Tuunainen, A. Spangar, P. von Lode, K. Rantakokko-Jalava, G. Otto, S. Scheding, T. Soukka, S. Wittfooth, and T. Laurell, "Integrated acoustic separation, enrichment, and microchip polymerase chain reaction detection of bacteria from blood for rapid sepsis diagnostics," Anal. Chem. **88**(19), 9403–9411 (2016).

[7] P. Augustsson, C. Magnusson, M. Nordin, H. Lilja, and T. Laurell, "Microfluidic, label-free enrichment of prostate cancer cells in blood based on acoustophoresis," Anal. Chem. **84**(18), 7954–7962 (2012).

[8] R. Zmijan, U. S. Jonnalagadda, D. Carugo, Y. Kochi, E. Lemm, G. Packham, M. Hill, and P. Glynne-Jones, "High throughput imaging cytometer with acoustic focussing," RSC Adv. **5**(101), 83206–83216 (2015).

[9] M. Ohlin, I. Iranmanesh, A. E. Christakou, and M. Wiklund, "Temperature-controlled mpa-pressure ultrasonic cell manipulation in a microfluidic chip," Lab Chip **15**(16), 3341–3349 (2015).

[10] P. Thevoz, J. D. Adams, H. Shea, H. Bruus, and H. T. Soh, "Acoustophoretic synchronization of mammalian cells in microchannels," Anal. Chem. **82**(7), 3094–3098 (2010).

[11] D. J. Collins, B. Morahan, J. Garcia-Bustos, C. Doerig, M. Plebanski, and A. Neild, "Two-dimensional single-cell patterning with one cell per well driven by surface acoustic waves," Nat. Commun. **6**, 8686 (2015).

[12] F. Guo, Z. Mao, Y. Chen, Z. Xie, J. P. Lata, P. Li, L. Ren, J. Liu, J. Yang, M. Dao, S. Suresh, and T. J. Huang, "Three-dimensional manipulation of single cells using surface acoustic waves," Proc. Natl. Acad. Sci. U.S.A. **113**(6), 1522–1527 (2016).

[13] P. Augustsson, J. T. Karlsen, H.-W. Su, H. Bruus, and J. Voldman, "Iso-acoustic focusing of cells for size-insensitive acousto-mechanical phenotyping," Nat. Commun. **7**, 11556 (2016).

[14] G. Sitters, D. Kamsma, G. Thalhammer, M. Ritsch-Marte, E. J. G. Peterman, and G. J. L. Wuite, "Acoustic force spectroscopy," Nat. Meth. **12**(1), 47–50 (2015).

[15] B. W. Drinkwater, "Dynamic-field devices for the ultrasonic manipulation of microparticles," Lab Chip **16**, 2360–2375 (2016).

[16] D. J. Collins, C. Devendran, Z. Ma, J. W. Ng, A. Neild, and Y. Ai, "Acoustic tweezers via sub-time-of-flight regime surface acoustic waves," Sci. Adv. **2**(7), e1600089 (2016).

[17] H. G. Lim, Y. Li, M.-Y. Lin, C. Yoon, C. Lee, H. Jung, R. H. Chow, and K. K. Shung, "Calibration of trapping force on cell-size objects from ultrahigh-frequency single-beam acoustic tweezer," IEEE Trans. Ultrason. Ferr. **63**(11), 1988–1995 (2016).

[18] D. Baresch, J.-L. Thomas, and R. Marchiano, "Observation of a single-beam gradient force acoustical trap for elastic particles: Acoustical tweezers," Phys. Rev. Lett. **116**, 024301 (2016).

[19] B. Hammarström, B. Nilson, T. Laurell, J. Nilsson, and S. Ekström, "Acoustic trapping for bacteria identification in positive blood cultures with MALDI-TOF MS," Anal. Chem. **86**(21), 10560–10567 (2014).

[20] A. Lenshof, M. Evander, T. Laurell, and J. Nilsson, "Acoustofluidics 5: Building microfluflidic acoustic resonators," Lab Chip **12**, 684–695 (2012).

[21] P. Reichert, D. Deshmukh, L. Lebovitz, and J. Dual, "Thin film piezoelectrics for bulk acoustic wave (BAW) acoustophoresis," Lab Chip **18**(23), 3655–3667 (2018).

[22] R. P. Moiseyenko and H. Bruus, "Whole-system ultrasound resonances as the basis for acoustophoresis in all-polymer microfluidic devices," Phys. Rev. Appl. **11**, 014014 (2019).

[23] W. N. Bodé, L. Jiang, T. Laurell, and H. Bruus, "Microparticle acoustophoresis in aluminum-based acoustofluidic devices with PDMS covers," Micromachines **11**(3), 292 (2020).

[24] M. Dubois and P. Muralt, "Properties of aluminum nitride thin films for piezoelectric transducers and microwave filter applications," Appl. Phys. Lett. **74**(20), 3032–3034 (1999).

[25] A. De Pastina, D. Maillard, and L. Villanueva, "Fabrication of suspended microchannel resonators with integrated piezoelectric transduction," Microelectron. Eng. **192**, 83–87 (2018).

[26] G. Piazza, P. J. Stephanou, and A. P. Pisano, "Piezoelectric aluminum nitride vibrating contour-mode MEMS resonators," J. Microelectromech. Syst. **15**(6), 1406–1418 (2006).

[27]U. Zaghloul and G. Piazza, "Highly scalable NEMS relays with stress-tuned switching voltage using piezoelectric buckling actuators," IEEE Trans. Electron. Dev. **61**(10), 3520–3528 (2014).

[28]N. Sinha, G. E. Wabiszewski, R. Mahameed, V. V. Felmetsger, S. M. Tanner, R. W. Carpick, and G. Piazza, "Piezoelectric aluminum nitride nanoelectromechanical actuators," Appl. Phys. Lett. **95**(5), 053106 (2009).

[29]R. H. Olsson III, K. E. Wojciechowski, M. S. Baker, M. R. Tuck, and J. G. Fleming, "Post-CMOS-compatible aluminum nitride resonant MEMS accelerometers," J. Microelectromech. Syst. **18**(3), 671–678 (2009).

[30]H. Zhang, W. Pang, H. Yu, and E. S. Kim, "High-tone bulk acoustic resonators on sapphire, crystal quartz, fused silica, and silicon substrates," J. Appl. Phys. **99**(12), 124911 (2006).

[31]J. Masson, G. Martin, R. Boudot, Y. Gruson, S. Ballandras, A. Artieda, P. Muralt, B. Belgacem, and L. Chomeloux, "On the dispersive behaviour of AlN/Si high overtone bulk acoustic resonators," in *2007 IEEE International Frequency Control Symposium Joint with the 21st European Frequency and Time Forum* (2007), pp. 741–744.

[32]T. Fujikura, O. Matsuda, D. M. Profunser, O. B. Wright, J. Masson, and S. Ballandras, "Real-time imaging of acoustic waves on a bulk acoustic resonator," Appl. Phys. Lett. **93**(26), 261101 (2008).

[33]R. Ruby, "The 'how & why' a deceptively simple acoustic resonator became the basis of a multi-billion dollar industry," in *2017 IEEE 30th International Conference on Micro Electro Mechanical Systems (MEMS)* (2017), pp. 308–313.

[34]N. R. Skov, J. S. Bach, B. G. Winckelmann, and H. Bruus, "3D modeling of acoustofluidics in a liquid-filled cavity including streaming, viscous boundary layers, surrounding solids, and a piezoelectric transducer," AIMS Math. **4**, 99–111 (2019).

[35]N. R. Skov, P. Sehgal, B. J. Kirby, and H. Bruus, "Three-dimensional numerical modeling of surface-acoustic-wave devices: Acoustophoresis of micro- and nanoparticles including streaming," Phys. Rev. Appl. **12**, 044028 (2019).

[36]P. Augustsson, R. Barnkob, S. T. Wereley, H. Bruus, and T. Laurell, "Automated and temperature-controlled micro-PIV measurements enabling long-term-stable microchannel acoustophoresis characterization," Lab Chip **11**(24), 4152–4164 (2011).

[37]J. S. Bach and H. Bruus, "Theory of pressure acoustics with viscous boundary layers and streaming in curved elastic cavities," J. Acoust. Soc. Am. **144**, 766–784 (2018).

[38]See supplementary material at https://www.scitation.org/doi/suppl/10.1121/10.0005624 for details on the values of the material parameters, focus time t_{foc}, and animations of the resonance modes.

[39]P. Hahn and J. Dual, "A numerically efficient damping model for acoustic resonances in microfluidic cavities," Phys. Fluids **27**, 062005 (2015).

[40]L. P. Gorkov, "On the forces acting on a small particle in an acoustical field in an ideal fluid," Sov. Phys.–Dokl. **6**(9), 773–775 (1962) [Dokl. Akad. Nauk SSSR **140**, 88–91 (1961)].

[41]M. Settnes and H. Bruus, "Forces acting on a small particle in an acoustical field in a viscous fluid," Phys. Rev. E **85**, 016327 (2012).

[42]R. Barnkob, P. Augustsson, T. Laurell, and H. Bruus, "Measuring the local pressure amplitude in microchannel acoustophoresis," Lab Chip **10**(5), 563–570 (2010).

[43]P. B. Muller, M. Rossi, A. G. Marin, R. Barnkob, P. Augustsson, T. Laurell, C. J. Kähler, and H. Bruus, "Ultrasound-induced acoustophoretic motion of microparticles in three dimensions," Phys. Rev. E **88**(2), 023006 (2013).

[44]A. G. Steckel, H. Bruus, P. Muralt, and R. Matloub, "Fabrication, characterization, and simulation of glass devices with AlN thin-film transducers for excitation of ultrasound resonances," Phys. Rev. Appl. **16**, 014014 (2021).

[45]COMSOL Multiphysics 5.4 (2018), available at http://www.comsol.com (Last viewed 16 June 2021).

[46]W. N. Bodé and H. Bruus, "Numerical study of the coupling layer between transducer and chip in acoustofluidic devices," J. Acoust. Soc. Am. **149**(5), 3096–3105 (2021).